

Ultrashort Pulsed Laser Surface Patterning of Titanium to Improve Osseointegration of Dental Implants

Christoph Zwahr,* Alexander Welle, Tobias Weingärtner, Christiane Heinemann, Benjamin Kruppke, Nikolai Gulow, Marzellus große Holthaus, and Andrés Fabián Lasagni

Ultrashort pulsed direct laser interference patterning (DLIP) is used to generate hierarchical line-like patterns on titanium surfaces to control cell adhesion and spreading on dental implants, thereby improving osseointegration. The DLIP structures have spatial periods of 3, 5, 10, and 17 μm . They are produced using a laser source with a pulse duration of 10 ps and cumulated energy densities between 0.1 and 78.9 J cm^{-2} . Laser-induced periodic surface structures (LIPSS) and submicron features are obtained on the treated samples. The DLIP treatment leads to the development of a thick titanium oxide layer, which is imaged and quantified using time-of-flight secondary ion mass spectrometry (ToF-SIMS). Several days (30–56) after the laser treatment, specimens with larger spatial periods are hydrophilic, whereas samples with spatial periods of 3 μm are hydrophobic. Seeded human osteoblasts on the laser-structured samples show 2.5 times higher cell numbers after 7 days in vitro culture compared with osteoblasts on a grit-blasted and etched reference sample. Finally, cell adhesion to a structured 3D dental implant is demonstrated.

They concluded that the bone response is influenced by the surface topography in the micrometer range, and that samples with moderate surface roughness (S_a) between 1 and 2 μm show the best performance. In addition, some publications suggested a positive influence of surfaces presenting a hierarchical micro- and nanometer topography.^[5–8]

Mendes et al. studied doubly etched Ti surfaces coated with calcium phosphate crystals having a nominal size range of 20–100 nm. Coated and uncoated samples were tested in a rodent model. Nine days after implantation in the distal femur, the bone directly proximal and distal to the implant was removed, resulting in a test sample comprising the implant with two attached cortical arches. The harvested bone/implant samples were subjected to a tensile test and the recorded disruption


1. Introduction

The surface topography and chemistry of titanium dental implants have a high impact on the healing progress of the implant in the surrounding bone tissue. A surface roughness in the micrometer and submicrometer range generally leads to higher proliferation of cells as well as improved protein synthesis compared with a flat surface.^[1–3] Wennerberg and Albrektsson analyzed 100 research papers to review the effect of the titanium surface topography on bone integration.^[4]

force showed that the coated samples had significantly greater disruption forces than the uncoated samples.^[5] Meirelles et al. drew similar conclusions from their observations on modified electropolished cylinders and blasted screw-shaped implants with calcium phosphate nanoparticles and nanometer TiO_2 coatings. In a rabbit model, enhanced bone formation has been demonstrated for nanostructured implants, whether modified with calcium phosphate or TiO_2 .^[6–8] In addition, the presence of a sufficiently thick titanium oxide (TiO_2) layer was found to be important, because it can pacify tissue-destroying agents

C. Zwahr, Prof. A. Fabián Lasagni
Institute of Manufacturing Technology
Technische Universität Dresden
George-Bähr Str. 3c, 01069 Dresden, Germany
E-mail: christoph.zwahr@tu-dresden.de

C. Zwahr, Prof. A. Fabián Lasagni
Fraunhofer-Institut für Werkstoff- und Strahltechnik (IWS)
Winterbergstraße 28, 01277 Dresden, Germany

 The ORCID identification number(s) for the author(s) of this article can be found under <https://doi.org/10.1002/adem.201900639>.

© 2019 The Authors. Published by WILEY-VCH Verlag GmbH & Co. KGaA, Weinheim. This is an open access article under the terms of the Creative Commons Attribution License, which permits use, distribution and reproduction in any medium, provided the original work is properly cited.

DOI: 10.1002/adem.201900639

Dr. A. Welle, T. Weingärtner
Karlsruhe Nano Micro Facility
Karlsruher Institut für Technologie
Hermann-von-Helmholtz-Platz 1, 76344 Eggenstein-Leopoldshafen, Germany

Dr. C. Heinemann, Dr. B. Kruppke
Institute of Materials Science, Max Bergmann Center of Biomaterials
Technische Universität Dresden
Budapester Str. 27, 01069 Dresden, Germany

N. Gulow, Dr. M. g. Holthaus
BEGO Implant Systems GmbH & Co. KG
Wilhelm-Herbst-Str. 1, 28359 Bremen, Germany

immediately after implantation.^[9] For conventional titanium-based implants used in dental surgery, the thickness of a natural Ti oxide layer increases from 5 to 200 nm within 6 years in vivo.^[10,11] This porous oxide layer is of great importance because it allows the incorporation of calcium and phosphorus ions improving osseointegration. In contrast, faulty implants are shown to have a thin Ti oxide layer, having, after several years, the same thickness as in the first days of implantation or even less.^[9,12,13]

Various techniques have been used in the past to modify the surface topography of titanium dental implants. The most widely used method is sand/grain blasting with various materials of controlled size distribution, followed by acid etching to reach an average surface roughness S_a of 1–2 μm .^[14] However, the treated surfaces need an additional cleaning step for the removal of used particles and the toxic etching solution. As one-step fabrication methods, different technologies such as stand-alone acid etching, anodization, plasma spraying, and laser ablation methods were investigated in the past.^[4,14–21] Recently, we published a study about improving the biological performance of titanium dental implants using direct laser interference patterning (DLIP) with a nanosecond pulsed laser system.^[22] In that study, line-like interference patterns achieved by the overlapping of two laser beams were produced on Ti grade 4 samples. On the line-like structures, the cell viability of human osteoblasts (hOBs) was 16% higher as compared with a grit-blasted and acid-etched reference. However, pulsed laser systems offer the possibility to produce hierarchical surface patterns using two-beam DLIP. Especially, ultrashort pulsed laser processing can induce the formation of periodic ripples, which are known as laser-induced periodic surface structures (LIPSS).^[23,24] When created with polarized laser radiation, these ripples can have a periodicity close to the laser wavelength and are generally oriented orthogonally to the polarization vector. Ripples having these properties are referred to as low-spatial frequency LIPSS (LSFLs). Within these structure features, usually also ripples with a periodicity smaller than the laser radiation can be produced, termed high-spatial frequency LIPSS (HSFLs). Therefore, the developed topography using two-beam DLIP has an entirely different characteristic compared with surfaces treated by nanosecond pulses. Therefore, the developed topography using two-beam DLIP has an entirely different characteristic compared with surfaces treated by nanosecond pulses.

In this study, both flat blanks and screw-shaped implants machined from pure titanium (grade 4) are patterned using two-beam DLIP with a pulsed picosecond laser system. The angle between the laser beams is varied to obtain line-like patterns with spatial periods in the range of 3–17 μm . The resulting topography and morphology are analyzed by confocal microscopy and scanning electron microscopy (SEM). The titanium reactive layer is analyzed by time-of-flight secondary ion mass spectrometry (ToF-SIMS). To compare the potential of this technology for improving osseointegration, the adhesion and proliferation of hOBs cells are evaluated on both, the picosecond laser-treated surfaces as well as on reference grit blasted and etched surfaces. Possible changes in the surface energy on the bulk material resulting from laser-structuring process are evaluated by measuring the static contact angles of the surfaces using the sessile drop method.

2. Results and Discussion

As mentioned in Section 1, line-like DLIP structures, produced by applying a nanosecond pulsed laser system, have shown promising results concerning the improvement of cell proliferation and viability.^[22] To study the influence of additional topographical features that can be simultaneously produced with ultrashort pulsed lasers, pure titanium (grade 4) substrates were processed using similar spatial periods to further improve cell proliferation and cell adhesion. The size of the spatial periods used in this work was chosen based on the typical average size of osteoblasts cells (20–30 μm) and in accordance with previous publications.^[25] For instance, line-like periodic structures produced with a spatial period of 20 μm have already shown the capability to improve cell viability.^[22] In this context, the largest structure period selected was 17 μm , being close to the osteoblast cell size. In addition, structures with smaller feature sizes, Ti surfaces with 3 and 10 μm periods, were produced to analyze the adhesion of osteoblasts. For the treatment of implants, a spatial period of $\approx 5 \mu\text{m}$ was chosen, to demonstrate the capability of the developed optical configuration to structure 3D geometries. This selected period is technically more challenging as compared with larger periods (e.g., 10 or 17 μm), as the interference volume size decreases with larger angles required for overlapping the laser beams to obtain the interference pattern (see Section 4). Regarding the geometry of the structures, the line-like patterns were chosen not only because they have already shown to improve cell viability, but also because they can be produced much easier and faster compared with other geometries using DLIP. In addition, studies by Ricci and coworkers, were also based on dental implants processed with line-like geometries, showing enhanced tissue integration in clinical studies.^[26,27]

The spatial period Λ was controlled by varying the angle α between the interfering beams (see Section 4). Using this approach, spatial periods of $\Lambda = 3 \mu\text{m}$, $\Lambda = 5 \mu\text{m}$, $\Lambda = 10 \mu\text{m}$, and $\Lambda = 17 \mu\text{m}$ were achieved for angles of $\alpha = 10.21^\circ$, $\alpha = 6.11^\circ$, $\alpha = 3.05^\circ$, and $\alpha = 1.69^\circ$, respectively. Furthermore, the structure height h of the periodic patterns can be controlled by the cumulated fluence F_{cum} . The evolution of the structure height as function of the cumulated laser fluence in the range of 0.1 to 78.9 J cm^{-2} is shown in **Figure 1** for the 3, 10, and 17 μm spatial periods. For the 10 and 17 μm period, a linear increase of the average structure height with increasing cumulated fluence was measured (Figure 1b,c). The maximal structure heights for the 10 and 17 μm periods were $h = 2.1 \pm 0.1 \mu\text{m}$ at $F_{\text{cum}} = 50.0 \text{ J cm}^{-2}$, and $h = 1.9 \pm 0.4 \mu\text{m}$ at $F_{\text{cum}} = 57.2 \text{ J cm}^{-2}$. Also in case of the 3 μm pattern, a linear increase with the cumulated fluence up to $h = 1.9 \pm 0.2 \mu\text{m}$ at $F_{\text{cum}} = 40.0 \text{ J cm}^{-2}$ was observed. However, a further increase in the cumulative fluence did not lead to a significant increase in the average structure height (Figure 1a). The reason for this behavior can be related to the high aspect ratio (AR) of these structures, defined as h/Λ . As the maximal obtained heights were similar for all used spatial periods, the AR for the structures with the smaller period are significantly higher as compared with the larger periods (AR = 0.7 for $\Lambda = 3 \mu\text{m}$; AR = 0.2 for $\Lambda = 10 \mu\text{m}$; AR = 0.1 for $\Lambda = 17 \mu\text{m}$). In consequence, high ARs can prevent the laser light from reaching the structure valleys, thus reducing the efficiency of the ablation process. This could also explain why no limitation in the structure

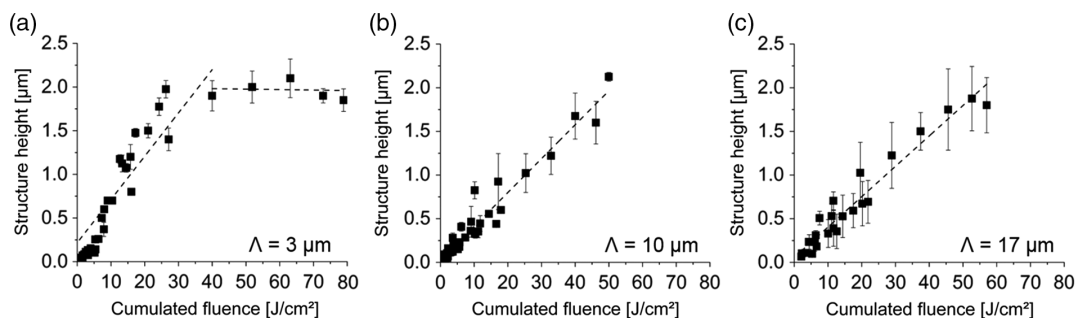


Figure 1. Structure height analysis of line-like DLIP patterns depending on the used cumulated fluence for spatial periods of a) 3 μm , b) 10 μm , and c) 17 μm .

height was reached for the larger spatial periods in the examined cumulative fluence interval.

To obtain comparable topographies in terms of structure heights and ARs with our previous study, samples with structure heights between 0.4 and 1.8 μm were used for cell adhesion tests. The parameters used to produce these samples are shown in **Table 1**. The final average surface roughness, S_a , and maximum surface height, S_z , of the laser-processed samples are also indicated in the table, showing variations between 0.19 ± 0.02 to 0.84 ± 0.12 and 3.3 ± 0.5 to 7.9 ± 0.4 μm , respectively.

SEM images of the laser-processed samples are shown in **Figure 2**. In each panel, an optical image of the macroscopic appearance of the processed samples is included as inset. Moreover, the optical image of the untreated reference surface is also shown in Figure 2a (left view of the inset: untreated reference; right view of the inset: laser-processed Ti sample). As shown in Figure 2, the laser-treated samples exhibit a significant variation of their optical appearance. The observed color variation can be related to both the growth of an oxide layer during the laser treatment and a light-trapping effect induced by the micro-/nanotopographical features.^[28–30] In the lower cumulated fluence regime (Figures 2a,c,e), all samples have a matt gray finish aspect after the laser treatment, independently of the used spatial period. However, an increase of the energy input leads to a significant change in the color appearance for all spatial periods. While the color changes from gray (Figure 2a) to black for the 3 μm period (Figure 2b), samples treated with larger spatial periods turn to blue tones (Figure 2d,f).

According to Antończak et al., the bluish colors are produced by interference effects that are related with the growth of an oxide

layer on the Ti samples. Its thickness is controlled by the total deposited laser energy. Differently, the black tonalities are related to light-trapping effects, which are stronger for surfaces showing features with high ARs. In consequence, the sample with the shortest spatial period and the highest AR (AR = 0.7 for $\Lambda = 3$ μm , Figure 2b) is significantly darker than the flatter surfaces (AR = 0.1 for $\Lambda = 17$ μm , Figure 2f).

In addition to the line-like periodic DLIP patterns, smaller features were also produced on the laser-affected areas. In particular, on the surfaces, treated at lower cumulative fluence (Figure 2a,c,e), wavy patterns with a spacing of ≈ 0.8 μm are observed. These structures are oriented perpendicular to the polarization of the laser beam. Considering their size, orientation, and the used laser wavelength of 1064 nm, these features can be identified as LSFLs.^[24] These patterns have also been observed in the past in combination with DLIP structures on stainless steel surfaces, using ps laser pulses.^[31]

The inset in the upper right of Figure 2c shows the magnification of the area indicated with a black frame in the original image. Here, another periodic array is visible, which is aligned parallel to the beam polarization in between the LSFL pattern. These structures are significantly smaller than the LSFL features, with a repetitive distance of approximately 150 nm. In this case, based on their size, orientation, and periodicity, they can be classified as HSFLs.^[24] As shown in Figure 2c,e, the LIPSS features are present on both the interference maxima (valleys) and the interference minima (peaks).

From Figure 2b,d,f, it can also be discerned that in the higher cumulated fluence range, the topographies of the structures appear to be roughened, and deeper grooves interrupt the

Table 1. Laser parameters for structuring Ti samples for final adhesion tests and the resulting structure heights and surface roughness values and relative oxide levels from SIMS depth profiles.

Period [μm]	Fluence [J cm^{-2}]	Overlap [%]	Cumulated fluence [J cm^{-2}]	Structure height [μm]	S_a [μm]	S_z [μm]	Relative oxide level, ^{18}O SIMS data [%]
3	0.79	95.0	16	1.3 ± 0.2	0.21 ± 0.01	3.3 ± 0.5	0.43
		99.0	79	1.8 ± 0.5	0.84 ± 0.12	7.9 ± 0.4	1.00
10	0.56	95.0	11	0.7 ± 0.1	0.21 ± 0.01	3.3 ± 0.5	0.40
		98.9	50	1.4 ± 0.3	0.47 ± 0.01	5.7 ± 0.4	0.63
17	0.66	94.6	12	0.4 ± 0.1	0.19 ± 0.02	3.7 ± 0.2	0.25
		98.8	57	1.7 ± 0.5	0.58 ± 0.01	5.3 ± 0.4	0.89

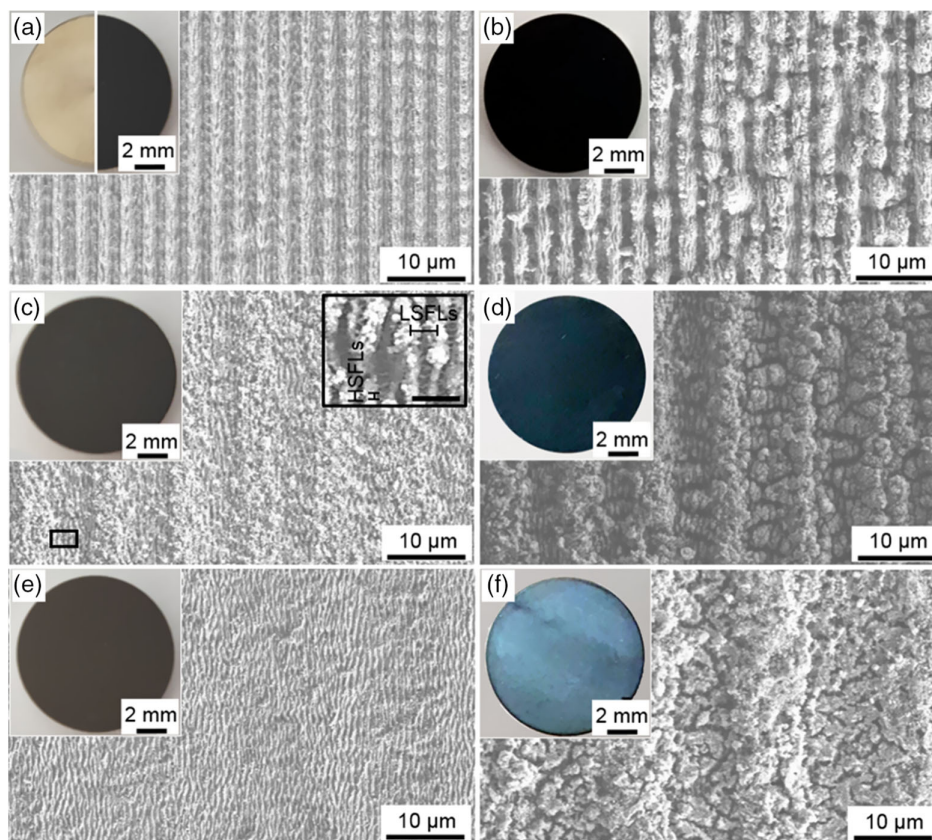


Figure 2. SEM and macroscopic pictures of DLIP-structured titanium surfaces with a,b) 3 μm , c,d) 10 μm , and e,f) 17 μm spatial period. a,c,e) Samples irradiated with lower cumulated fluences between 11 and 16 J cm^{-2} and the right samples irradiated with higher cumulated fluences between 50 and 79 J cm^{-2} . The bright specimen shown in the inset of (a) is the native Ti disc. In the inset, LSFLs and HSFLs are highlighted. The scale corresponds to 1 μm .

continuous line-like DLIP structure. The grooves are also an ultrashort pulse phenomenon that occurs by applying many pulses and forms in the direction parallel to the polarization with a periodicity larger than the laser wavelength.^[32] It is discussed that their formation is due to an inhomogeneous absorption of the laser light below a rough surface. However, this process is not fully understood.^[23] Furthermore, some particles in the lower micrometer and submicrometer range are especially visible on the peaks of the structures. They can be ablation products that mainly arise from the interference maxima positions, which are derived toward the interference minimum positions due to the recoil pressure that arises during the laser–material interaction process.^[33]

To better visualize the morphology of the LIPSS features on the DLIP pattern together with possible effects induced by the laser treatment, a cross section of the 17 μm spatial period sample was obtained from focused ion beam sectioning. This sample was irradiated with a cumulated fluence of $F_{\text{cum}} = 57 \text{ J cm}^{-2}$, and the obtained SEM image is shown in **Figure 3**. Because of the large spatial period related to the DLIP process, the produced LIPSS at different positions (e.g., interference maxima and minima) are clearly shown. Furthermore, because of the high cumulative fluence chosen, morphology alterations are more pronounced based on the thicker oxide layer being formed.

Figure 3a shows the cross section of the Ti samples with two interference peaks, which are covered by smaller features. The larger peaks were formed by DLIP structuring, whereas the smaller features are the LSFLs. In particular, in Figure 3b, LIPSS are visible on both the DLIP peaks and valleys.

The height of the LIPSS measured in this cross section is about $0.7 \pm 0.1 \mu\text{m}$, which corresponds to an AR of 0.9. The high magnification SEM image of Figure 3c also shows, at the DLIP peak (corresponding to the interference minima positions), a thick reactive layer on top of the LIPSS. This layer can be recognized by the difference in brightness, due to backscatter effects where heavier species (e.g., Ti) appear brighter than lighter ones (e.g., O). The electron diffraction spectroscopy (EDS) measurements performed at both positions showed a concentration of $96 \pm 1\%$ Ti and $3 \pm 1\%$ O in the lighter and $71 \pm 14\%$ Ti and $29 \pm 14\%$ O in the darker areas (indicated by “bulk titanium” and “oxide layer”). As the thick oxide layer has been found at the interference minima position, it should be caused by deposited ablation products that have oxidized in the atmosphere. This hypothesis is strengthened by the fact that any visible oxide layer has been found on the right DLIP valleys, which correspond to the interference maxima positions.

The surface chemistry of the samples was further analyzed using ToF-SIMS. With ToF-SIMS, it is possible to visualize the

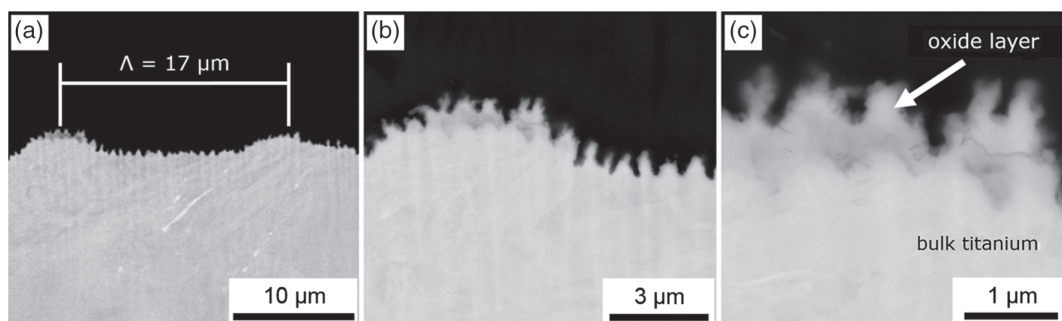


Figure 3. Focused ion beam-polished cross section of a Ti surface structured with $17\text{ }\mu\text{m}$ spatial period at $F = 57\text{ J cm}^{-2}$. a) Two peaks of the DLIP structure. b,c) Higher magnifications of the left peak in (a). b) LIPSS in the structure valley and peak are visible with a spatial period of $\Lambda = 0.8\text{ }\mu\text{m}$ and structure height of $h = 0.7 \pm 0.1\text{ }\mu\text{m}$. c) Thick oxide layer is visible on top of the structure peak indicated by an arrow.

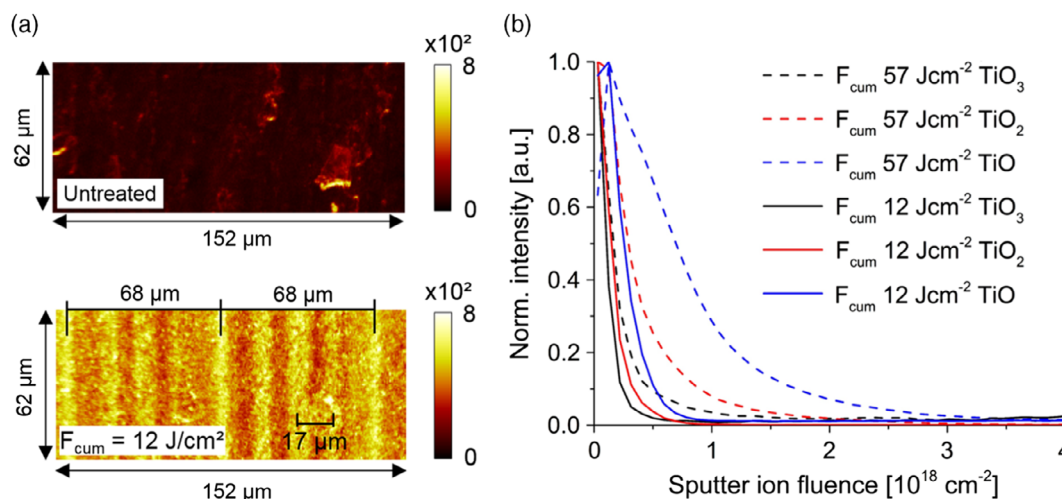


Figure 4. ToF-SIMS measurements on an untreated reference and a DLIP-structured surface with $\Lambda = 17\text{ }\mu\text{m}$ treated at $F = 12\text{ J cm}^{-2}$. a) Depth-integrated top views of the lateral oxygen distribution on an untreated and laser-structured surface. b) Relative intensities of three titanium oxide clusters plotted against the fluence of the applied Cs-sputtering ions. As the fluence increases deeper layers of the surface are analyzed. Solid lines: DLIP-structured surface with $\Lambda = 17\text{ }\mu\text{m}$, $F_{\text{cum}} = 57\text{ J cm}^{-2}$; dashed lines: DLIP-structured surface with $\Lambda = 17\text{ }\mu\text{m}$, $F_{\text{cum}} = 12\text{ J cm}^{-2}$. SIMS data acquired from a $150 \times 150\text{ }\mu\text{m}^2$ field of view.

lateral distribution of chemical compounds with a resolution in the submicrometer range. In **Figure 4a**, the depth-integrated lateral oxygen distribution on the untreated reference and a laser-treated sample with $17\text{ }\mu\text{m}$ spatial period, irradiated with $F_{\text{cum}} = 12\text{ J cm}^{-2}$, is shown. A line-wise alternating oxygen content was observed on the structured sample, with oxygen rich lines following the laser intensity pattern with a spatial period of $17\text{ }\mu\text{m}$. Another superordinate periodical distribution of the oxygen content is visible regarding the applied hatch distance d_H (see Section 4, and Figure S6b, Supporting Information) of $68\text{ }\mu\text{m}$ between adjacent-structured DLIP tracks. The oxygen rich lines vary in width and intensity, possibly due to the Gaussian intensity distribution of the laser beam (spot size of the laser beams was about $130\text{ }\mu\text{m}$). The interference maxima in the center of the Gaussian beam have the highest laser intensity. The higher the laser intensity, the more material is removed and the higher the recoil pressure directing the material toward the interference minima positions.^[33]

Therefore, oxides are formed predominantly along the interference minima. Figure 4b shows depth profiles of both $17\text{ }\mu\text{m}$

patterned samples with high and low F_{cum} . These data are obtained by eroding the sample with 2 keV Cs^+ ions and taking individual secondary ion mass spectra from a $150 \times 150\text{ }\mu\text{m}^2$ field of view. The fluence of the applied Cs ions plotted on the x-axis is an arbitrary depth scale. As can be seen, different titanium oxo clusters are detected in SIMS. All of them are decreasing in intensity as deeper layers of the samples are reached. The concentration of TiO_3^- , being the oxygen richest ion found, is decreasing rather fast as compared with TiO_2^- , TiO^- , and Ti_2O^- . Several important limitations on SIMS experiments have to be considered: 1) Sputter cleaned titanium, much like sublimated titanium, is a very active getter material readily reacting with oxygen and other residual gasses in the recipient. Care was taken to perform all experiments at good ultrahigh vacuum conditions at $2\text{--}5 \times 10^{-9}\text{ mbar}$, and maximum erosion speed, but even so the oxidation of titanium is fast enough that a residual oxygen level was detected even a longest erosion times. However, this residual oxygen level is in the range of 1–2% of the maximum oxygen level detected at the sample surface in the laser-induced titanium oxide layer; 2) There is a critical mass

overlap between TiO_3 , 95.9332 m/z , and Ti_2 , 95.8964 m/z . Both peaks are not fully baseline separated. In consequence, there is a slight crosstalk in the metallic bulk regime of the depth profiles where a rather strong Ti_2 signal, only detected in this layer, effects an artifact reading for the TiO_3^- signal; 3) Recording negative polarity secondary ion (SI) spectra with Cs erosion results in detector saturation for species with high ionization yields, in this case, ^{16}O . To allow for a correct relative quantification of the overall (depth-integrated) oxygen content of the samples, the less abundant oxygen isotope ^{18}O was used. Figure S1, Supporting Information, shows the depth profile of the ^{18}O signal for differently treated samples. As shown, the thickness of the titanium oxide layer is dependent on the applied laser treatment: whereas in the nontreated reference sample (Figure S1, black line, Supporting Information), the native oxide layer is very thin and the ^{18}O signal is dropping abruptly upon the onset of erosion, all laser-processed samples show a much thicker oxide layer being in general more pronounced for the three high laser fluence samples. Integrating the oxygen signals over depth, results in the relative oxygen levels given in Table 1, rightmost column. Given the importance of a porous oxide layer for the incorporation of calcium and phosphorus ions and thus the adhesion of natural bone tissue without implant encapsulation in fibrous tissue, the enriched oxide layer could be of great interest for an improved healing of a dental implant.^[9]

Regarding the phase composition of the enriched oxide layer, the research of Yang et al. can be considered, who present a detailed analysis about the phase composition of pure titanium surfaces irradiated by fs, ps, and ms laser pulses.^[34] They analyzed the oxide layer using X-ray photoelectron spectroscopy (XPS) and transmission electron microscopy (TEM) methods. For 10 ps pulses, major compositions of the laser ablation product were TiO_2 , TiO_2 rutile, Ti_2O_3 , TiN , Ti , and $\text{TiO}_{0.73}$. Compared with fs pulses, the content of residual elemental titanium (Ti) is gradually reduced. This could mainly result from a relatively full reaction between air and titanium during picosecond pulse duration compared with the femtosecond laser ablation. For ms pulses, TiO_2 (in oxide films) and TiO_2 rutile become the major components. Based on the TEM analysis results, it was deduced that a polycrystalline structure and amorphous structure are the main structural components of the picosecond laser and titanium ablation product, and the proportion of amorphous structure is higher between these two structures.

In our previous study on ns-structured titanium surfaces, XPS showed an increase of nitrogen to 20 ± 3 at% over the 4 at% reference value on an unstructured sample. Here, with ToF-SIMS, CN^- secondary ions were detected in the very first surface layers on the unstructured and ps-structured surfaces. The CN^- signal follows the depth dependence of TiO_3^- . Thus, it can be concluded that it is partially derived from titanium nitride and adventitious carbon contaminations. The titanium nitride level increases by factor 3 when comparing laser structured with native samples. Consequently, the ps laser treatment also leads to an increase of N in the titanium-reactive layer.

As the adsorption of proteins onto the surface of a biomaterial is an important initial event triggering cellular host responses, and this physisorption process is strongly dependent on the wettability of the substrate, water contact angles (WCAs) of the processed samples were measured. The adhesion of osteoblasts on

the Ti surface is determined by the interaction between the extracellular matrix of these cells and the protein layer formed on the surface. Hydrophilic surfaces do not alter the conformation of adsorbed proteins and keep the proteins in a less denaturated state.^[35–37] The contact angle measurements performed on the laser-structured samples and on untreated reference are presented in Figure S2, Supporting Information. Due to the shape of the DLIP line-like structures, anisotropic droplet formation occurs on the surfaces, so that the contact angles were measured parallel and perpendicular to the valleys. At the unstructured reference, a WCA of $86^\circ \pm 7^\circ$ was measured being typical for the used Ti material.^[22] However, for clean titanium surfaces, the WCAs should be less than 40° .^[38] The difference in contact angle is due to a hydrophobic coating of hydrocarbons that forms over time on the Ti surfaces from air-borne contaminations.^[22,38,39] On samples with spatial periods of 10 and 17 μm , the WCAs were measured 30 days after laser processing. As shown in Figure S1, Supporting Information, they range from $16^\circ \pm 2^\circ$ to $74^\circ \pm 8^\circ$ measured parallel to the valleys and from $29^\circ \pm 4^\circ$ to $83^\circ \pm 2^\circ$ perpendicular to the valleys, which is less than the one measured on reference. The reduction of the WCAs can be explained using the Wenzel model.^[40] Based on the Wenzel model, the contact angle θ on a textured surface can be calculated using Equation (1)

$$\cos(\theta) = R_f \cos(\theta_0) \quad (1)$$

where the surface roughness factor R_f can be calculated using Equation (2) and θ_0 is the measured contact angle on the smooth surface^[22,41]

$$R_f = 1 + 2 \frac{h}{\Lambda} \quad (2)$$

The calculated roughness factors between 1.04 and 1.28 for samples with 10 and 17 μm periods should lead to WCAs of 85° – 86° (for $\theta_0 = 86^\circ$ as determined on the reference sample). This could explain the WCA measured on samples with a spatial period of 17 μm and low structure height, but is unsatisfactory for the other patterns studied. The reason for the lower WCAs measured on the other samples could be, that the development of the hydrocarbon layer was not yet complete and, more important, the change in surface chemistry of the Ti reactive layer.

On the Ti surfaces corresponding to the 3 μm line-like structures, hydrophobic WCAs were measured 56 days after laser treatment. In average, they range between 123° and 132° . The water droplets are isotropically shaped. The hydrophobicity of the samples can be explained in this case by the Cassie–Baxter model, which describes the contact angle for a liquid on a composite surface.^[42] In a two-component system, wherein one component is air having a contact angle of 180° to the liquid, the effective contact angle θ can be calculated using Equation (3)

$$\cos(\theta) = \varphi_s \cos(\theta_0) - (1 - \varphi_s) \quad (3)$$

where φ_s is the fraction of the solid–liquid contact. Air pockets are retained under the water droplet in case of those samples exhibiting higher ARs of 0.4 and 0.7, compared with the samples with larger spatial periods. Using this model with $\varphi_s = 0.5$ and

$\theta_0 = 86^\circ$, a contact angle of $\theta = 118^\circ$ can be calculated for the spatial period of $3\ \mu\text{m}$, which is in good agreement with the measured values (123° – 132°).

Finally, in vitro cell proliferation tests with hOBs were performed on the laser-treated surfaces to verify the potential of the ultrashort DLIP method to improve osseointegration. As a reference, standard grit-blasted and etched samples (TiPure^{Plus}, Bego Implant Systems) with a surface roughness of $S_a = 1.26\ \mu\text{m}$ were used. In comparison, the DLIP-treated surfaces exhibited lower average surface roughness (Table 1). **Figure 5** shows fluorescence microscopic images of cell adhesion after 7 days on grit-blasted, acid-etched, and DLIP-structured surfaces with spatial periods of 3, 10 and $17\ \mu\text{m}$. The structure heights were $h = 1.3 \pm 0.2$, $h = 1.4 \pm 0.3$, and $h = 1.7 \pm 0.5$ for the spatial periods of $3\ \mu\text{m}$ (low F_{cum}), $10\ \mu\text{m}$ (high F_{cum}), and $17\ \mu\text{m}$ (high F_{cum}), respectively. As it can be seen, the cells attached and spread randomly on the reference surface (Figure 5a), whereas on all structured surfaces, they were aligned parallel to the direction of the microvalleys (Figure 5b–d). This effect (contact guidance) was already reported in previous studies and in this case, the structures did not significantly influence the course of osteogenesis.^[22,43,44]

However, a considerable difference in the metabolism and cell proliferation was observed on the standard processed to the laser-structured samples. The lactate dehydrogenase (LDH) activity was measured and linearly correlated in control experiments with the cell number. First, the colonization efficiency of hOBs was measured after 24 h on all Ti samples, with values between 30% and 40% (see Figure S3, Supporting Information). The cell density on the grit-blasted and acid-etched reference was set to a relative amount of $100\% \pm 11\%$ (see **Figure 6**). For all DLIP-treated samples, the average, relative amount of cells was higher in comparison with the reference, ranging from $140\% \pm 40\%$ ($\Lambda = 10\ \mu\text{m}$, low F_{cum} , with $h = 0.7 \pm 0.1\ \mu\text{m}$) to $250 \pm 70\%$ ($\Lambda = 17\ \mu\text{m}$, low F_{cum} , with

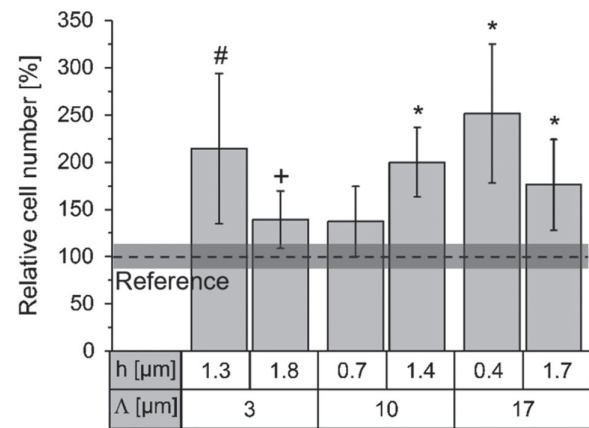


Figure 6. Cell number on titanium samples after 7 days in cultivation medium as determined by LDH activity measurement. Cell number is demonstrated with respect to the grit-blasted and acid-etched reference set to 100% (Reference). Statistical significance compared with Ti Pure samples is marked with an asterisk (*) at a p -value of ≤ 0.05 and with # and + at p -values of ≤ 0.06 and ≤ 0.07 , respectively.

$h = 0.4 \pm 0.1\ \mu\text{m}$). The statistical data were analyzed using an ANOVA test, the null hypothesis being that the laser structuring has no influence on the cell adhesion of hOBs compared with the standard process. In this test, a p -value of ≤ 0.05 should be strong evidence against the null hypothesis to reject it.

In the cell culture experiments after 7 days, the data of the sample group with $\Lambda = 10\ \mu\text{m}$ and $h = 1.4 \pm 0.3\ \mu\text{m}$ and both sample groups with $\Lambda = 17\ \mu\text{m}$ had a p -value of less than or equal to 0.05. The data of the sample groups with $3\ \mu\text{m}$ spatial period had p -values of 0.06 ($h = 1.3 \pm 0.2\ \mu\text{m}$) and 0.07 ($h = 1.8 \pm 0.5\ \mu\text{m}$) and are considered to be marginal as they are close to the cut-off of 0.05. Only samples with a spatial period of $10\ \mu\text{m}$ and lower

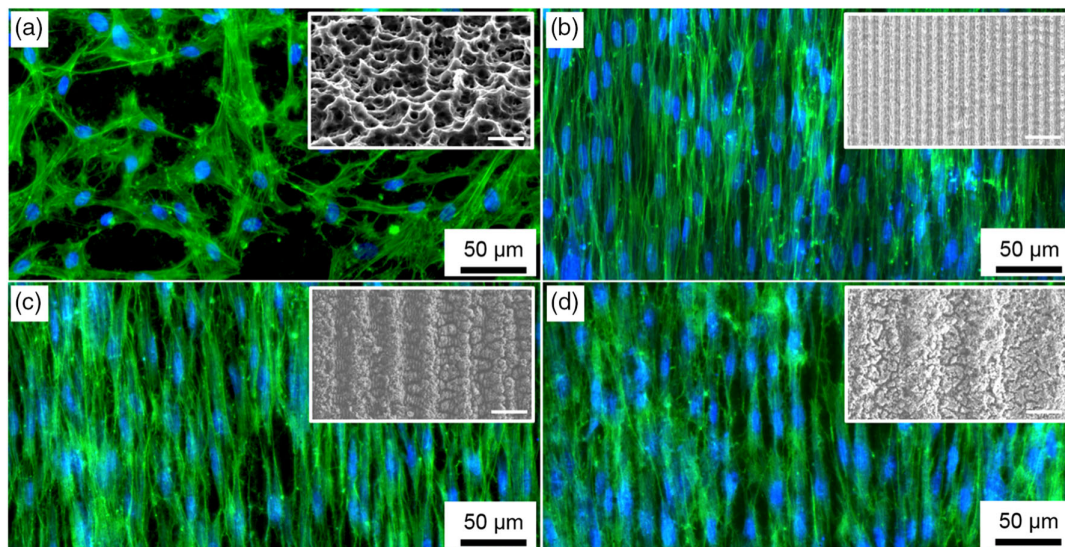


Figure 5. Fluorescence microscopic images of adhered hOBs on titanium surfaces after 7 days in cultivation medium. The insets show corresponding SEM images of the surface with a scale bar corresponding to $10\ \mu\text{m}$. a) Cells on a grit-blasted and acid-etched reference with $S_a = 1.26\ \mu\text{m}$, b–d) cells on line-like patterns with $3\ \mu\text{m}$ ($h = 1.3 \pm 0.2\ \mu\text{m}$), $10\ \mu\text{m}$ ($h = 1.4 \pm 0.3\ \mu\text{m}$), and $17\ \mu\text{m}$ ($h = 1.7 \pm 0.5\ \mu\text{m}$) spatial periods, respectively. Actin staining is shown in green and cell nuclei in blue.

structure height of $h = 0.7 \pm 0.1 \mu\text{m}$ showed no statistically significant improvement in cell adhesion when compared with grit-blasted and acid-etched reference.

While for ns laser radiation no increase in the number of cells compared with the grit-blasted and etched reference was measured, in this case, the laser treatment led to an increased cell adhesion and proliferation.^[22] This could be caused by the changed structure morphology due to LIPSS formation and deposition of submicron particles caused by the ablation process. The cell-surface interaction was examined more in detail taking SEM images of osteoblasts placed on grit-blasted and acid-etched as well as laser-structured surfaces for 7 days in cultivation medium (Figure 7). On the reference surface (Figure 7a), the osteoblasts are easy to recognize due to their light appearance compared with the titanium surface. The cells are largely separated and have a polygonal shape. In contrast, the osteoblasts on the laser-structured surfaces with $\Lambda = 3 \mu\text{m}$ and $h = 1.3 \pm 0.2 \mu\text{m}$ (Figure 7b), $\Lambda = 10 \mu\text{m}$ and $h = 1.4 \pm 0.3 \mu\text{m}$ (Figure 7c), and $\Lambda = 17 \mu\text{m}$ and $h = 1.7 \pm 0.5 \mu\text{m}$ (Figure 7d) are difficult to distinguish from the surfaces. The cell bodies are flattened and merge with the neighboring cells. Therefore, the cells cannot be viewed separately.

In the insets in Figure 7b,c, long protrusions of the cells are visible, serving as mechanical linkages to the substrate surfaces. The cell protrusions form contact points to the surface, which are on the sample with $10 \mu\text{m}$ line-like structure randomly connected everywhere. On the surface with spatial period of $3 \mu\text{m}$, the contact points are almost exclusively connected to the DLIP structure peaks (interference minima). This could be due to the small spatial period and the relatively high AR of 0.4. Because cells are larger than the DLIP valleys, they cannot penetrate them.

Thus, they adhere on the DLIP peaks and connect to the neighboring peaks with the contact points. Therefore, the possible adhesion points are limited, and fewer cells can adhere, compared with the larger patterns.

In Figure S4, Supporting Information, an area on a sample with $\Lambda = 10 \mu\text{m}$ and $h = 0.7 \pm 0.1 \mu\text{m}$ structure height, in which cells have reached maximum confluency and cover the entire surface is shown. Due to the dense colonization, the cells no longer aligned to the microvalleys and grew at an angle of about 45° over them. Although in LDH assay, no significant increase in the number of cells was measured on this pattern, this spread of cells and the development of many contact points are indicators of a truly good cell adhesion, which was not observed on the reference samples.^[45–47]

To summarize the important aspects of the laser treatment to reach a better bone response, the following statements can be made. The surface topography which was modified by the DLIP treatment and in addition presents LIPSS features (and thus producing hierarchical surface patterns) can directly lead to better adhesion and higher proliferation of cells as it is known from other publications. This surface has also shown to be more hydrophilic compared with the untreated reference, as well as to have a thick oxide layer, which probably can improve the healing progress of the implant in the bone tissue as well as the long-term preservation of the implant in the body. In addition, the presence of the titanium oxide layer (TiO_2) can inhibit tissue-destroying agents immediately after implantation. The hydrophilic wetting behavior is relevant, as the adhesion of osteoblasts on the Ti surface is determined by the interaction between the extracellular matrix of cells and the protein layer on the surface. Furthermore, hydrophilic surfaces preserve the native

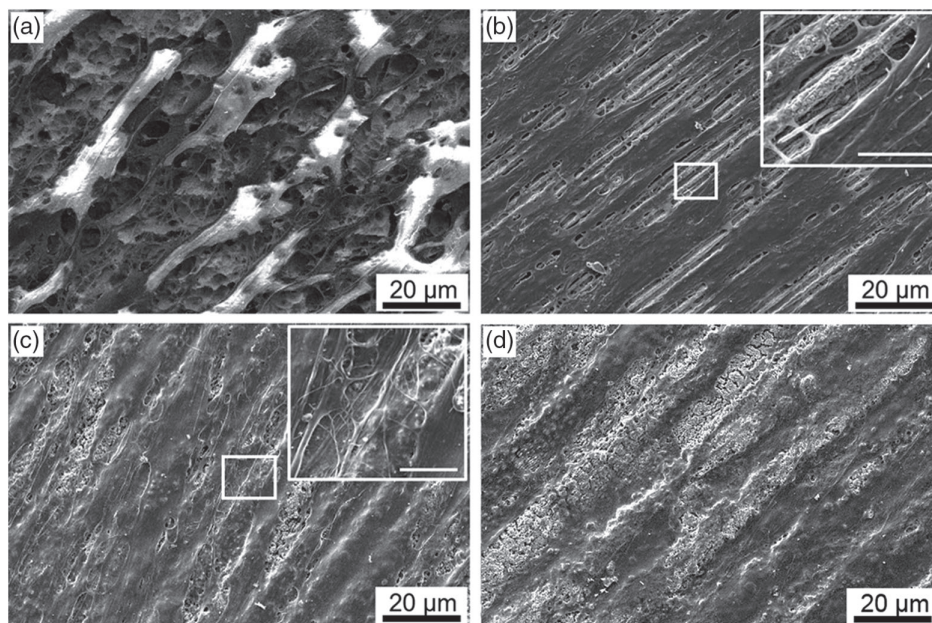


Figure 7. SEM images of adhered hOBs on titanium surfaces after 7 days in vitro. a) Cells on a grit-blasted and acid-etched reference with $S_a = 1.26 \mu\text{m}$. b) Cells on a line-like patterns with $3 \mu\text{m}$ ($h = 1.3 \pm 0.2$) spatial period. The lower part of the image shows osteoblasts adhered on samples with c) $10 \mu\text{m}$ and d) $17 \mu\text{m}$ spatial periods, and structure heights of $h = 1.4 \pm 0.3$ and $h = 1.7 \pm 0.5 \mu\text{m}$, respectively. The insets in the pictures show the contact points of the osteoblasts on the surfaces with scale bars corresponding to $5 \mu\text{m}$.

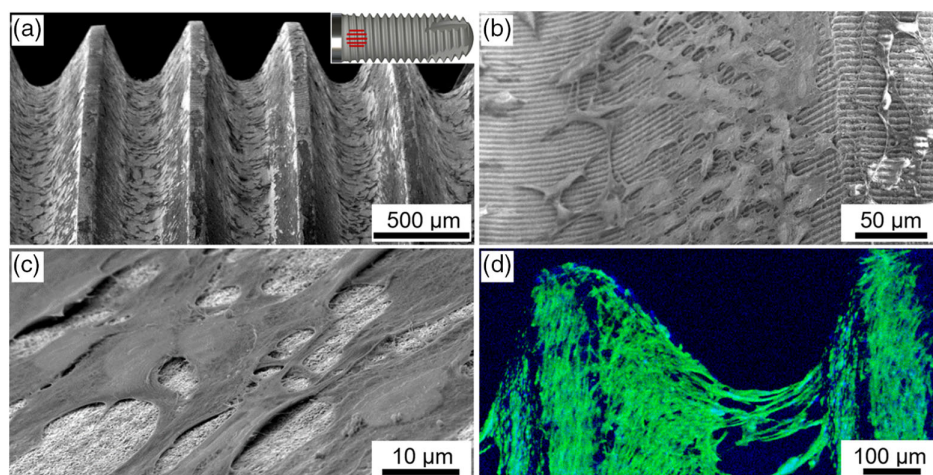


Figure 8. Cell adhesion on a DLIP-patterned 3D Ti dental implant with a 5 μm spatial period cumulated fluence of 16 J cm^{-2} . a–c) SEM images of the implant with adherent osteoblasts on the surface. The inset in (a) shows a model of the implant with the orientation of the line-like DLIP pattern. d) CLSM image with adhered osteoblasts on the dental implant with actin staining (green) and nucleus staining (blue).

conformation of adsorbed proteins resulting in a protein layer enhancing cell adhesion.

Finally, 3D-shaped titanium dental implants were structured using the diffractive optical element (DOE) setup described in Section 4. In this case, the spatial selected period was 5 μm and a cumulated fluence of $F_{\text{cum}} = 16 \text{ J cm}^{-2}$ was used. The relative small spatial period was selected, as the size of the interference volume is much smaller compared with largest periods (see Section 4). Thus, this condition is more unfavorable for the DLIP treatment, representing a challenge for processing 3D parts. **Figure 8a–c** shows SEM images of the treated dental implant using DLIP method. From the images (especially from **Figure 8b**), it can be seen that the 5 μm DLIP structure was produced over the whole irradiated surface, denoting that the interference volume was larger than the size of the screw's thread. Furthermore, on the implant surface, a structure height of $h = 1.7 \pm 0.2 \mu\text{m}$ was measured. In consequence, the capability of the system to structure 3D geometries was demonstrated. Human osteoblasts were grown on one of the samples for 7 days to demonstrate cell adhesion on a real implant surface (**Figure 8** and **Figure S5**, Supporting Information). As was the case for the cylindrical test samples, the cells orientated parallel to the micro-valleys on areas with less cell adhesion and spread over the micro pattern on areas with a high density of cells.

3. Conclusion

Titanium grade 4 substrates were treated using an ultrashort pulse DLIP process, to create hierarchical surfaces that enhance cell adhesion and proliferation of hOBs. Using the DLIP method with a two-beam interference optics, line-like patterns with spatial periods between 3 and 17 μm were produced. By varying the laser fluence and the pulse number (and thus the cumulated laser fluence), the morphology of the patterns was controlled. The ultrashort pulse treatment with 10 ps pulse duration also causes the development of LIPSS features (LSFLs and HSFLs) with spatial periods around 800 nm (LSFLs) and 150 nm (HSFLs).

The ToF-SIMS measurements revealed an up to sevenfold increase of the oxide level on the laser-structured samples compared with the untreated reference.

The amount of cells was up to 2.5 times higher after 7 days in cultivation medium on DLIP-structured surface than on grit-blasted and acid-etched surfaces, which was also statistically proven. The better cell adhesion was also demonstrated by a spread of cells and the development of many contact points on the laser-structured samples compared with the reference. Finally, dental implant surfaces were patterned vertically to the thread and cultured for 7 days with hOB, demonstrating cell adhesion on real implant surfaces. For future animal and clinical studies, the obtained hierarchical DLIP/LIPSS structure in combination with its hydrophilic wetting behavior as well as the produced oxide layer could have a high impact on the healing progress of the implant in the bone tissue as well as improving its long-term preservation in the body.

4. Experimental Section

Sample Preparation: As substrate material titanium grade 4-turned blanks with a diameter of 11 mm and a thickness of 1.6 mm were used. Samples were cut-off by turning process using a biocompatible cooling liquid and then cleaned in pure ethyl alcohol and rinsed twice with demineralized water using ultrasonic cleaning for 10 min each. To verify the removal of the coolant, EDS measurements were done on the titanium surfaces. To protect them from contamination and mechanical damage, the samples were then shrink-wrapped with bacteria proof and heat sealable polyester-polypropylene foil MELAfol (EN 868-5) from MELAG Medizintechnik. Before and after the laser treatment, all substrates were cleaned in pure ethyl alcohol ($\text{C}_2\text{H}_5\text{OH}$) for 5 min in ultrasonic bath.

Direct Laser Interference Patterning: Periodic patterns were generated using a pulsed Nd:YVO₄ solid-state laser system (PX200–3–GH, Edgewave) with a fundamental wavelength of 1064 nm, a pulse duration of 10 ps, and a pulse repetition rate of 1 kHz. The incident beam was split by a DOE into its diffraction orders, where about 79% of the power was equally distributed to the two first diffraction orders (see **Figure S6a**, Supporting Information). The first diffraction orders were collimated using a prism and finally recombined with an aspheric lens. Detailed information about the experimental setup has been published in previous studies.^[48]

The interference of the two laser beams caused a line-like intensity modulation, which is given by Equation (4)

$$\Phi(x, y) = 4\Phi_0 \cos^2\left(kx \sin \frac{\alpha}{2}\right) \quad (4)$$

where Φ_0 is the laser fluence of each beam, α is the angle of incidence between the interfering beams, and $k = 2\pi\lambda^{-1}$ is the wave number at the laser wavelength λ . The half intersection angle between the beams α defined the pitch Λ between two intensity maxima of the structure which is given by Equation (5).

$$\Lambda = \frac{\lambda}{2 \sin \alpha} \quad (5)$$

The structure depth and morphology were controlled by the laser fluence and the pulse overlap alone, which were varied from 0.11 to 0.79 J cm⁻² and from 0.0% to 99.0% (equivalent to a pulse number of 1–100 pulses). This resulted in cumulated fluences F_{cum} , defined as the product of the laser fluence and pulse number, between 0.1 and 78.9 J cm⁻². By overlapping interference areas parallel to the DLIP lines, a DLIP track was generated. The hatch distance d_H determined the space between adjacent structured tracks and was kept to about 50% of the diameter of the interference area for each period. A schematic view of the line-like patterning strategy is shown in Figure S6b, Supporting Information.

Surface Topography Characterization: The surface morphology was analyzed using both, a scanning electron microscope (ZEISS Supra 40VP) and a confocal microscope (Sensofar S Neox). In the case of the confocal microscopy analyses, a 50× magnification objective was used, having a lateral and vertical resolutions of 170 and 3 nm, respectively.

Surface Chemistry Characterization: The chemical composition of the treated and untreated Ti substrates was analyzed using ToF-SIMS. ToF-SIMS was performed on a TOF.SIMS5 instrument (ION-TOF GmbH, Münster, Germany). This spectrometer was equipped with a Bi cluster primary ion source and a reflectron-type time-of-flight analyzer. Ultra-high vacuum (UHV) base pressure was <10⁻⁸ mbar. For high mass resolution, the Bi source was operated in “high current bunched” mode providing short Bi⁺ primary ion pulses at 25 keV energy. The short pulse length of 1 ns allowed for high mass resolution and unambiguous chemical assignments. For high lateral resolution, the source was operated in a non-bunched mode (bust alignment) to avoid chromatic aberration. For depth profiling, a dual beam analysis was performed in interlaced mode: The primary ion source was again operated in the nonbunched mode with a scanned area of 150 × 150 μm² (128 × 128 data points) and a sputter gun (operated with Cs⁺ ions, 2 keV, scanned over a concentric field of 300 × 300 μm², target current 150 nA) was applied to erode the sample. Cs implantation increased the ionization yield of negatively charged secondary ions like O⁻ and TiO⁻. As ¹⁸O yielded very strong signals, exceeding the dynamic range of the detector, ¹⁸O (0.2% natural abundance) was used for quantification instead, see Table 1. As sputtered titanium surface were exceptionally good getter substances for oxygen from the residual gases in the UHV system, data acquisition was performed at pressures below 5 × 10⁻⁹ mbar and a constant background count rate was corrected for. According to calculations by Yamamura and Tawara, a Cs fluence of 10¹⁷ 1/cm² at 45° to the sample surface would erode pure titanium to a depth of 30–35 nm.^[49] However, the sputter yield of titanium oxide can differ and was not determined experimentally as the specimen did not show a sharp interface between oxide and pure metal.

Cross-Sectional Analysis: The microstructure of a laser-treated titanium sample ($\Lambda = 17 \mu\text{m}$) was displayed performing reactive ion etching with a IB-09101 CP polisher from Jeol GmbH. An acceleration voltage of 6 kV and a maximum ion current of 186 μA were used to transversely polish the Ti samples.

Contact Angle Measurements: Static contact angle measurements were conducted using a DSA 100 S Drop Shape Analyzer (Krüss GmbH). A drop of deionized water with a volume of 2 μL was put on the ethyl alcohol

cleaned Ti surfaces with a cannula of 0.52 mm diameter. Initially, the drop was constituted at the top of the cannula and then put on the plane surface. The analysis was done with Krüss Advance software and the “tangent” method.

Cell Culture: Cell culture experiments were using hOB (cryovial, Cat. No. 121 0311, Provitro GmbH, Berlin, Germany). The cells were cultivated in Dulbecco's modified Eagle medium (DMEM) supplemented with 10% fetal calf serum, 100 U mL⁻¹ penicillin and 100 μg mL⁻¹ streptomycin. Medium and all supplements were obtained from Merck Biochrom, Berlin, Germany. Prior to cell seeding, the Ti samples were placed in 48 well plates and incubated with culture medium for 24 h at 37 °C in a humidified incubator with 5% CO₂ and 95% air. After incubation, 5 × 10³ hOBs were seeded onto each Ti sample and cultivated up to 7 days.

A LDH cytotoxicity detection kit (Takara, Saint-Germain-en-Laye, France) was used to determine the cell number on the Ti samples. The measurements were performed with cell lysates obtained after 1 and 7 days of cultivation. Cell lysis was achieved with 1% Triton X-100 (Sigma) in phosphate-buffered saline (PBS). An aliquot of cell lysate was mixed with LDH substrate buffer and the enzymatic reaction was stopped after 30 min with 0.5 M HCl. The absorbance was read at 492 nm using a SpectraFluor Plus microplate reader (Tecan, Crailsheim, Germany). The LDH activity was correlated with the cell number using a calibration line of cell lysates with defined cell numbers.

Fluorescence microscopy and confocal laser scanning microscopy (CLSM) were applied to evaluate the cell morphology and orientation of hOB on Ti samples. After 7 days of cultivation, cell-seeded samples were fixed with 3.7% formaldehyde, and then permeabilized with 0.2% TritonX-100 in PBS. Cytoskeletal actin was stained with AlexaFluor 488-Phalloidin (Life Technologies) and cell nuclei with 4',6-diamidino-2-phenylindole (DAPI, Sigma). The staining was visualized using an upright Zeiss Axioscope 2 FS mot microscope (Jena, Germany) equipped with an AxioCam camera (Zeiss) and working with Axiovision Software. CLSM was performed with an LSM 510 META module (Zeiss) coupled to the Zeiss Axioscope 2 FS Mot microscope. Excitation of AlexaFluor 488 was carried out at 488 nm (Ar⁺ laser). The NIR-fs-laser was used for excitation of DAPI at 750 nm (two photon excitation) and fluorescence was recorded at 461 nm.

As preparation for the SEM investigation, cell-seeded Ti samples were dehydrated by a series of ethanol solutions of increasing concentration (10, 30, 50, 70, 80, 90, and 100%), infiltrated with hexamethyldisilazane (Fluka, Germany) and dried. Ti samples were mounted on stubs and coated with carbon in a Balzers SCD 050 coater. SEM was conducted using a Philips ESEM XL 30 scanning electron microscope working in high vacuum mode with 3 kV acceleration voltage.

Supporting Information

Supporting Information is available from the Wiley Online Library or from the author.

Acknowledgements

The work of A.F.L. and C.Z. was carried out in the framework of the Reinhart-Koselleck project (1323477257), which has received funding from the German Research Foundation (German: Deutsche Forschungsgemeinschaft DFG). Furthermore, this work was partially conducted with the support of the Karlsruhe Nano Micro Facility (KNMF), a Helmholtz Research Infrastructure at Karlsruhe Institute of Technology (KIT).

Conflict of Interest

The authors declare no conflict of interest.

Keywords

dental implants, direct laser interference patterning, osseointegration, surface functionalization, titanium

Received: May 27, 2019

Revised: September 4, 2019

Published online: October 25, 2019

- [1] B. Groessner-Schreiber, R. S. Tuan, *J. Cell Sci.* **1992**, 101, 209.
- [2] B. Isaacson, S. Jeyapalina, *Orthop. Res. Rev.* **2014**, 20, 55.
- [3] J. Raphael, M. Holodniy, S. B. Goodman, S. C. Heilshorn, *Biomaterials* **2016**, 84, 301.
- [4] A. Wennerberg, T. Albrektsson, *Clin. Oral Implant. Res.* **2009**, 20, 172.
- [5] V. C. Mendes, R. Moineddin, J. E. Davies, *Biomaterials* **2007**, 28, 4748.
- [6] L. Meirelles, A. Arvidsson, M. Andersson, P. Kjellin, T. Albrektsson, A. Wennerberg, *J. Biomed. Mater. Res. A* **2008**, 87, 299.
- [7] L. Meirelles, F. Currie, M. Jacobsson, T. Albrektsson, A. Wennerberg, *Int. J. Oral Maxillofac. Implants* **2008**, 23, 641.
- [8] L. Meirelles, L. Melin, T. Peltola, P. Kjellin, I. Kangasniemi, F. Currie, M. Andersson, T. Albrektsson, A. Wennerberg, *Clin. Implant Dentist. Relat. Res.* **2008**, 10, 245.
- [9] J. Mouhyi, D. M. Dohan Ehrenfest, T. Albrektsson, *Clin. Implant Dentist. Relat. Res.* **2012**, 14, 170.
- [10] D. McQueen, J. E. Sundgren, B. Ivarsson, I. Lundström, B. af Ekenstam, A. Svensson, P. I. Brånemark, T. Albrektsson, in *Clinical Applications of Biomaterials* (Eds: A.J.C. Lee, T. Albrektsson, P. I. Brånemark), Wiley, Chichester, UK **1982**, p. 179.
- [11] J.-E. Sundgren, P. Bodö, I. Lundström, *J. Colloid Interface Sci.* **1986**, 110, 9.
- [12] M. Esposito, J. Lausmaa, J.-M. Hirsch, P. Thomsen, *J. Biomed. Mater. Res.* **1999**, 48, 559.
- [13] M. Esposito, P. Thomsen, L. E. Ericson, U. Lekholm, *Int. J. Oral Maxillofac. Implants* **1999**, 14, 798.
- [14] R. Junker, A. Dimakis, M. Thoneick, J. A. Jansen, *Clin. Oral Implan. Res.* **2009**, 20, 185.
- [15] D. Kuczyńska-Zemła, P. Kwaśniak, A. Sotniczuk, M. Szychalski, P. Wieceński, J. Zdunek, R. Ostrowski, H. Garbacz, *Surf. Coat. Tech.* **2019**, 364, 422.
- [16] V. Babuska, J. Palan, J. Kolaja Dobra, V. Kulda, M. Duchek, J. Cerny, D. Hrusak, *Materials* **2018**, 11, 1827.
- [17] J. Frostevar, R. Olsson, J. Powell, A. Palmquist, R. Brånemark, *Appl. Surf. Sci.* **2019**, 485, 158.
- [18] A. M., O. Omar, W. Xia, A. Palmquist, in *Implant Dentistry - A Rapidly Evolving Practice* (Ed: I. Turkyilmaz), InTech, London, UK **2011**.
- [19] D. Buser, in *Titanium in Medicine* (Eds: D. M. Brunette, P. Tengvall, M. Textor, P. Thomsen), Springer, Berlin, Heidelberg **2001**, p. 875.
- [20] D. M. Dohan Ehrenfest, P. G. Coelho, B.-S. Kang, Y.-T. Sul, T. Albrektsson, *Trends Biotechnol.* **2010**, 28, 198.
- [21] S. Ferraris, A. Bobbio, M. Miola, S. Spriano, *Surf. Coat. Tech.* **2015**, 276, 374.
- [22] C. Zwahr, D. Günther, T. Brinkmann, N. Gulow, S. Oswald, M. Grosse Holthaus, A. F. Lasagni, *Adv. Healthc. Mater.* **2017**, 6, 1600858.
- [23] J. Z. P. Skolski, G. R. Römer, E. Bernardus, J. Vincenc Obona, V. Ocelik, A. J. Huis in 't Veld, J. T. M. de Hosson, *J. Laser Micro Nanoeng.* **2013**, 8, 1.
- [24] J. Z. P. Skolski, G. R. B. E. Römer, J. Vincenc Obona, A. J. Huis in 't Veld, *J. Appl. Phys.* **2014**, 115, 103102.
- [25] S. Puckett, R. Pareta, T. J. Webster, *Int. J. Nanomed.* **2008**, 3, 229.
- [26] J. L. Ricci, H. Alexander, *KEM* **2001**, 198-199, 179.
- [27] R. Guarnieri, R. Ceccarelli, J. L. Ricci, T. Testori, *Implant Dentist.* **2018**, 27, 81.
- [28] A. J. Antończak, B. Stępak, P. E. Koziół, K. M. Abramski, *Appl. Phys. A* **2014**, 115, 1003.
- [29] P. Fan, M. Zhong, L. Li, T. Huang, H. Zhang, *Optics Exp.* **2013**, 21, 11628.
- [30] A. Y. Vorobyev, C. Guo, *Appl. Phys. Lett.* **2008**, 92, 41914.
- [31] A. I. Aguilar-Morales, S. Alamri, A. F. Lasagni, *J. Mater. Process. Technol.* **2018**, 252, 313.
- [32] J. Bonse, J. Krüger, *J. Appl. Phys.* **2010**, 108, 34903.
- [33] M. D'Alessandria, A. Lasagni, F. Mücklich, *Appl. Surf. Sci.* **2008**, 255, 3210.
- [34] C. Yang, Y. Tian, L. Cui, D. Zhang, *Radiat. Eff. Defects Solids* **2015**, 170, 528.
- [35] B. Grössner-Schreiber, H. Terheyden, *Implantologie* **2004**, 12, 213.
- [36] M. Morra, *Water in Biomaterials Surface Science*, John Wiley & Sons, Chichester, UK **2001**.
- [37] C. Bischof, W. Possart, *Adhäsion: Theoretische und Experimentelle Grundlagen*, Akademie-Verlag, Berlin **1983**.
- [38] D. Scharnweber, F. Schlottig, S. Oswald, K. Becker, H. Worch, *J. Mater. Sci. Mater. Med.* **2010**, 21, 525.
- [39] A.-M. Kietzig, S. G. Hatzikiriakos, P. Englezos, *Langmuir* **2009**, 25, 4821.
- [40] R. N. Wenzel, *Industr. Eng. Chem.* **1936**, 28, 988.
- [41] M. Hans, C. Gachot, F. Müller, F. Mücklich, *Adv. Eng. Mater.* **2009**, 11, 795.
- [42] A. B. D. Cassie, S. Baxter, *Transact. Faraday Soc.* **1944**, 40, 546.
- [43] X. F. Walboomers, H. J. E. Croes, L. A. Ginsel, J. A. Jansen, *Biomaterials* **1998**, 19, 1861.
- [44] L. Prodanov, J. te Riet, E. Lamers, M. Domanski, R. Luttge, J. J. W. A. van Loon, J. A. Jansen, X. F. Walboomers, *Biomaterials* **2010**, 31, 7758.
- [45] G. Schneider, K. Burrige, *Exp. Cell Res.* **1994**, 214, 264.
- [46] M. A. Wozniak, K. Modzelewska, L. Kwong, P. J. Keely, *Biochim. Biophys. Acta* **2004**, 1692, 103.
- [47] H. Hendsi, M. F. Barbe, F. F. Safadi, M. A. Monroy, S. N. Popoff, *PLoS one* **2015**, 10, e0115325.
- [48] V. Lang, A. Rank, A. F. Lasagni, *Adv. Eng. Mater.* **2017**, 19, 1700126.
- [49] Y. Yamamura, H. Tawara, *At. Data Nucl. Data Tables* **1996**, 62, 149.